International Journal of Microwave and Wireless Technologies

cambridge.org/mrf

Metamaterial-based electromagnetically induced transparency-like sensor design with low-volume sliding dielectric loadings

Hasan Cetin[1,2,3] and Evren Ekmekci[1,2]

[1]Department of Electronics and Communication Engineering, Suleyman Demirel University, Isparta, Turkey; [2]Department of Electrical and Electronics Engineering, Suleyman Demirel University, Isparta, Turkey and [3]Department of Electrical and Electronics Engineering, Usak University, Usak, Turkey

Research Paper

Cite this article: Cetin H, Ekmekci E (2024) Metamaterial-based electromagnetically induced transparency-like sensor design with low-volume sliding dielectric loadings. *International Journal of Microwave and Wireless Technologies* **16**(2), 227–236. https://doi.org/10.1017/S175907872300079X

Received: 24 February 2022
Revised: 01 June 2023
Accepted: 02 June 2023

Keywords:
EIT-like metamaterial; low-volume dielectric sensing; tuning the EIT-like transmission window

Corresponding author: Evren Ekmekci, Email: evrenekmekci@sdu.edu.tr

Abstract

In this study, tunability of the electromagnetically induced transparency (EIT)-like transmission window by low-volume dielectric loadings is presented both numerically and experimentally in S-band. The EIT-like transmission behavior is obtained by a metamaterial, composed of an electric resonator and a closed-ring resonator patterned on a dielectric substrate. The frequency tuning is obtained by two applications called horizontal sliding application (HSA) and vertical sliding application based on sliding of the low-volume loadings from the edges to geometric center (i.e., inward). For both applications, the frequency tuning has been investigated for dielectric loadings which have relative permittivity of 2.2, 3, 4.5, and 6.15. The results reveal that the proposed sliding applications are effective on tuning the transmission peak frequency. An achieved 1136 and 971 MHz absolute spectral shifts and corresponding 6.34% and 5.41% absolute sensitivities by simulations and measurements, respectively, are the best results which are obtained for HSA at 5 mm shift value. Moreover, 14.67% sensitivity is obtained in simulations for the complete dielectric loading on the resonator in response to the increase in refractive index from 1 to 1.5. It is believed that the proposed applications will contribute to the existent sensing studies.

Introduction

The phenomenon of obtaining a narrower spectral band of transmission in a relatively broad absorption spectrum (i.e., in opaque medium) is called electromagnetically induced transparency (EIT), and it is commonly explained by quantum interference effect [1–5]. In early studies, this phenomenon was seen in the three-level atomic systems which required relatively complex setups with cryogenic temperatures and high intensity laser requirements [4, 5]; however, it had drawn exceedingly attention after adapting to classical systems explained by mechanical oscillators and RLC circuits, and therefore it was called as the EIT-like effect [3–6]. Contingent to this new phenomenon, metamaterial counterparts with EIT-like effect were presented [4–7].

EIT-like phenomena obtained in metamaterial structure are generally realized with two methods: one is the trapped mode resonance [4, 8] and the other is a result of the coupling between dark mode, bright mode, quasi-dark mode, or any binary or ternary combination of them [9–15]. The trapped mode is possible to be produced by breaking structural symmetry and there becomes a weak coupling to the free space [8]. One of the second methods, bright mode-dark mode coupling, exists on the structures (1) having a bright mode resonance with a lower quality (Q) factor which can be excited directly by the incident wave, and (2) dark mode resonance with a larger Q-factor which get no interaction with incident wave and free space [10, 14]. EIT-like metamaterials are frequently used in on slow-light applications [16, 17], light storage [18], modulators [19, 20], and sensors [20–27] with an increasing interest.

In the literature, there are various sensing approaches for solid sample detection with relatively low permittivity range in microwaves [28–39]. An important number of them realize the sensing application by using microstrip line–coupled designs [28, 33–39] or a substrate integrated waveguide sensor design [29]. Moreover, differential sensor designs are also popular that need a second dielectric material or free-space medium as a reference for permittivity detection [30–33, 36, 38].

In this study, two different dielectric loading applications are studied on an EIT-like metamaterial design composed of the electric resonator (ER) and the closed-ring resonator (CRR) in both simulations and experiments. During the analyses, the effects of the dielectric loadings (i.e., the effects of their real part of relative permittivity) on the tunability of the transmission

window in terms of the transmission peak frequency f_0 and Q-factor are investigated. The CRR is a commonly used structure in EIT-like resonator designs [40, 41] as the bright mode resonator with its lower Q-factor in the operation band. On the other hand, the ER serves as a quasi-dark mode resonator in the design. ER is a well-known metamaterial structure [42–45] observed in various applications such as absorber [46–48], sensor [49], polarizer [50], and antenna [51] designs. However, its usage in an EIT-like metamaterial design appears in the conference paper presented by the authors of this study which establishes the early designs and the feasibility of this study in only simulations by using cubic dielectric loadings on the gap regions [15]. It can be noted here that ER is sometimes called an electric LC resonator in the literature [44, 45, 48–50]. The prominent novelties of this study are listed as follows:

- This study presents significantly extended analyses of reference [15] including newer designs adapted for S-band waveguide simulation and experimental setups, two new tuning applications based on sliding of low-volume dielectric loadings, a tuning application based on complete dielectric loadings on the top of the EIT-like metamaterial to reveal the effects of partial loading on the sensitivity, and further analyses including electric field distributions, surface current plots, Q-factor, and dependence of f_0 on the real part of relative permittivity.
- In this study, the proposed applications which are composed of sliding low-volume dielectric loadings on EIT-like metamaterial are new. The applications promise two practical approaches: (1) a displacement sensing by sliding the identical two low-volume dielectrics over the EIT-like metamaterial structure and (2) a low-volume dielectric sensing by fixing the positions of the loadings on the EIT-like structure and changing their dielectric constant.
- In literature, the sensing applications that EIT-like structures take part uses relatively larger sizes of dielectrics (i.e., material under test [MUT]) to cover the entire structure [5, 21, 52–57]. However, in this study, we use low-volume dielectric loadings which cover only a small fraction of the resonator structure.

Design and characterization setups

The schematic from top with design parameters, and the photograph of the proposed EIT-like structure are shown in Fig. 1. The metallic CRR and ER structures was patterned over Rogers RT/duroid® 5880 substrate with relative permittivity $\varepsilon_r = 2.2$ and dielectric loss tangent $\tan\delta = 0.0009$. Herein, the thickness of the dielectric substrate is 0.762 mm and the thickness of the metallic conductor (i.e., copper, modeled by conductivity of 58 MS/m) is 17.5 μm. The dimensions of the substrate and the structure are given as $L_x = 72.136$ mm, $L_y = 34.036$ mm, $l_{cv} = 24$ mm, $l_{ch} = 24$ mm, $l_{ev} = 10$ mm, $l_{eh} = 10$ mm, $w_c = 1$ mm, $w_l = 1$ mm, $l_s = 3$ mm, $g = 1$ mm.

The numerical analyses of the design are carried out by using CST Studio Suite® frequency domain solver by using the simulation setup, as shown in Fig. 2(a). Herein two waveguide ports are placed in the z-axis direction, and perfect electrical conductors ($E_t = 0$) are used as the boundary conditions in the remaining directions to limit the computational domain [58]. In simulations, the background medium is modeled by $\varepsilon_r = 1$ and $\mu_r = 1$. For the experimental process, the structure is placed inside the sample holder as shown in Fig. 2(b–d). As the description of the applications a series of photographs, each taken in the sample holder,

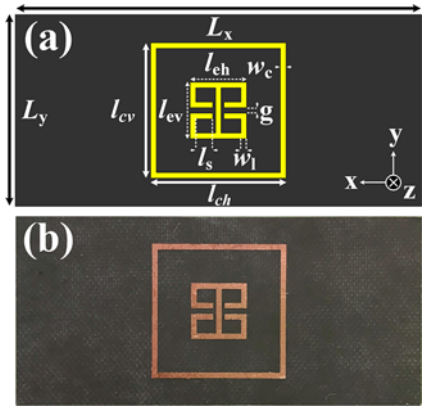

Figure 1. The studied EIT-like metamaterial design. (a) The schematic from top with design parameters. (b) The photograph of the fabricated structure.

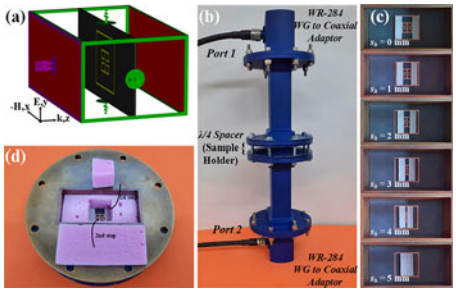

Figure 2. (a) Simulation and (b) experimental setups for EIT-like metamaterial characterization; (c) a series of photographs, each taken in the sample holder, illustrating the horizontal sliding application; and (d) the layout of EIT-like metamaterial together with dielectric loadings inside the sample holder with supporting pink XPS materials.

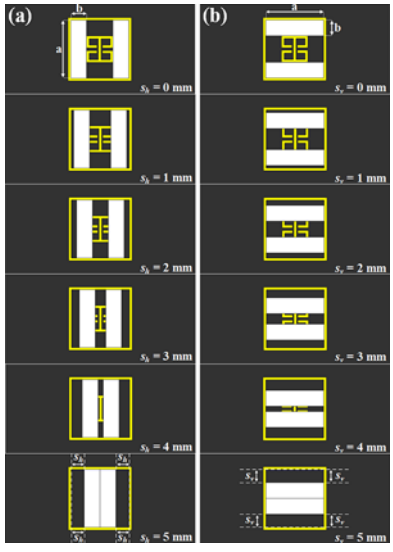

Figure 3. The schematic illustrations of the dielectric loading pairs composed of two identical $a \times b$ sized rectangular dielectric pieces in (a) horizontal sliding application and (b) vertical sliding application in six steps.

are presented in Fig. 3(c) illustrating the horizontal sliding application (HSA) as the example. During the experiments, to prevent the unwanted displacements of the dielectric loadings and to minimize the unwanted air gaps between the EIT-like metamaterial

https://doi.org/10.1017/S175907872300079X Published online by Cambridge University Press

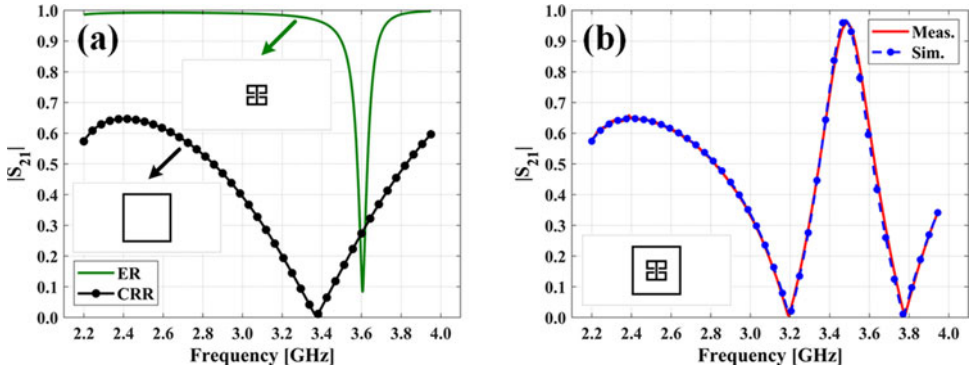

Figure 4. Transmission spectra of (a) individual ER and CRR structures in simulations and (b) EIT-like metamaterial in simulation and measurement.

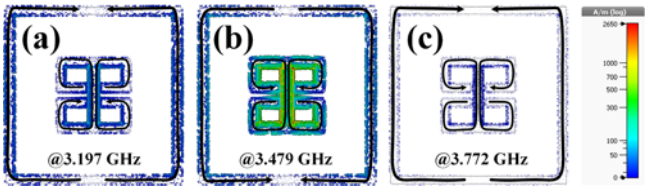

Figure 5. The surface current densities on EIT-like metamaterial structure. (a) At 3.197 GHz; the first transmission dip frequency, (b) at 3.479 GHz; the transmission peak frequency, and (c) at 3.772 GHz; the second transmission dip frequency.

and the dielectric loadings, extruded polystyrene (XPS) materials (i.e., pink foams observed in Fig. 2(d)) are used as support material. Our previous laboratory analyses revealed that effect of the XPS material might be negligible since it had similar dielectric properties with air [59]. Moreover, WR-284 coaxial to waveguide adaptors are used to connect the waveguide transmission line to the Agilent FieldFox N9926A vector network analyzer. Considering the cutoff frequencies of the first two propagating modes of a rectangular waveguide [60] together with the frequency band under investigation, only TE_{10} mode propagates in the simulation and experimental setups, where the wave propagation is along z direction, the electric field is along y direction, and the magnetic field is along x and z directions. However, the effects of H_z field, which has cosine variation [60], on the excitation of the structure may be neglected since the metallic structure is placed around the center of the waveguide cross section [61].

Figure 3 illustrates the two proposed dielectric loading mechanisms schematically, namely HSA and vertical sliding application (VSA) for tuning of the transmission window or tuning the of transmission peak frequency. HSA and VSA represent the applications where the loadings are positioned vertically and horizontally, respectively. As seen in the figure, the dielectric loadings are shifted gradually toward the geometric center of structure (i.e., inward) with the shift parameter s_h for HSA and s_v for VSA. For the proof of concept, the dielectric materials used as the dielectric loadings are uncladded Rogers RT/duroid® 5880 ($\varepsilon_r = 2.2$ and $\tan\delta = 0.0009$), Rogers CLTE-AT™ ($\varepsilon_r = 3$ and $\tan\delta = 0.0013$), Arlon AD450 ($\varepsilon_r = 4.5$ and $\tan\delta = 0.0035$), and Rogers RO4360G2™ ($\varepsilon_r = 6.15$ and $\tan\delta = 0.0038$) having thicknesses of 1.58, 1.524, 1.524, and 1.524 mm, respectively. During the analyses, the side lengths of the loadings are kept constant at $a = 22$ mm and $b = 6$ mm (see Fig. 3). In the simulations, the loadings are lifted as much as the metallic line thickness (i.e., 17.5 μm) to avoid any intersections between the dielectric loadings and the metallic resonator line. Considering the two proposed sliding applications; it can be said that it is important for the EIT-like metamaterial unit-cell to be symmetrical in the design along horizontal and vertical directions.

Results and discussion

The transmission (i.e., $|S_{21}|$) spectra of the individual unloaded (i.e., bare) CRR and ER structures in simulations and the unloaded EIT-like metamaterial structure in simulations and measurements are presented in Fig. 4(a) and (b), respectively. In Fig. 4(a), the individual CRR and ER are shown to possess a transmission dip at 3.372 and 3.607 GHz, respectively. On the other hand, the composition of them, i.e., the EIT-like metamaterial, has two transmission dips and one transmission peak in the frequency band of investigation. In more detail, the dips are observed at 3.197 and 3.772 GHz in simulations and observed at 3.193 and 3.779 GHz in measurements. In addition, the transmission peak frequency f_0 is observed at 3.479 GHz in simulation and at 3.484 GHz in measurement. Figure 4(b) reveals that the simulated and the measured transmission spectra agree very well. In the design, CRR and the ER have the role of the bright and the quasi-dark mode resonators, respectively.

To figure out the resonance behavior of the EIT-like metamaterial, the surface current densities are plotted at 3.197, 3.479, and 3.772 GHz, as shown in Fig. 5. The plots at each frequency support that the ER has circulating current densities, which is the identifier of an *LC* resonance [19, 22, 44] and the CRR has stronger surface currents at the vertical edges which are parallel to direction of the incident electric field vector; hence, this resonance can be described as an electric dipole resonance [40]. In all, the surface current densities are strongest at 3.479 GHz where the transmission peak is observed.

The $|S_{21}|$ plots regarding the tuning application for HSA at the shift values $s_h = 0$ mm and $s_h = 5$ mm, and for VSA at the shift values $s_v = 0$ mm and $s_v = 5$ mm are shown in Figs. 6 and 7, respectively. Since the transmission plots for s_h and s_v values from 2 to 4 present similar behaviors with the those observed for the extremes (i.e., 0 and 5 mm), the transmission spectra are only presented for 0 and 5 mm shift values for four dielectric loading cases together with the bare ones. However, all aggregate results will be discussed through Fig. 9.

In Figs. 6 and 7, the bare MUT designates the air which is chosen as the starting point of the permittivity level (i.e., $\varepsilon_r = 1$). For HSA at $s_h = 0$ mm, as the real part of relative permittivity of the MUT is increased from 1 to 6.15 (i.e., from bare to RO4360G2™), f_0 reduces from 3.479 to 3.175 GHz in simulations and from 3.484 to

https://doi.org/10.1017/S175907872300079X Published online by Cambridge University Press

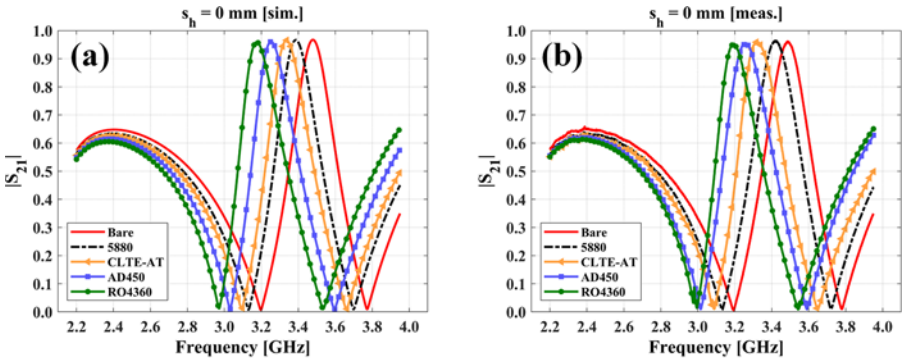

Figure 6. Transmission spectra of the bare and the dielectric-loaded EIT-like metamaterials in horizontal sliding application. (a) $s_h = 0$ mm simulations, (b) $s_h = 0$ mm measurements, (c) $s_h = 5$ mm simulations, and (d) $s_h = 5$ mm measurements.

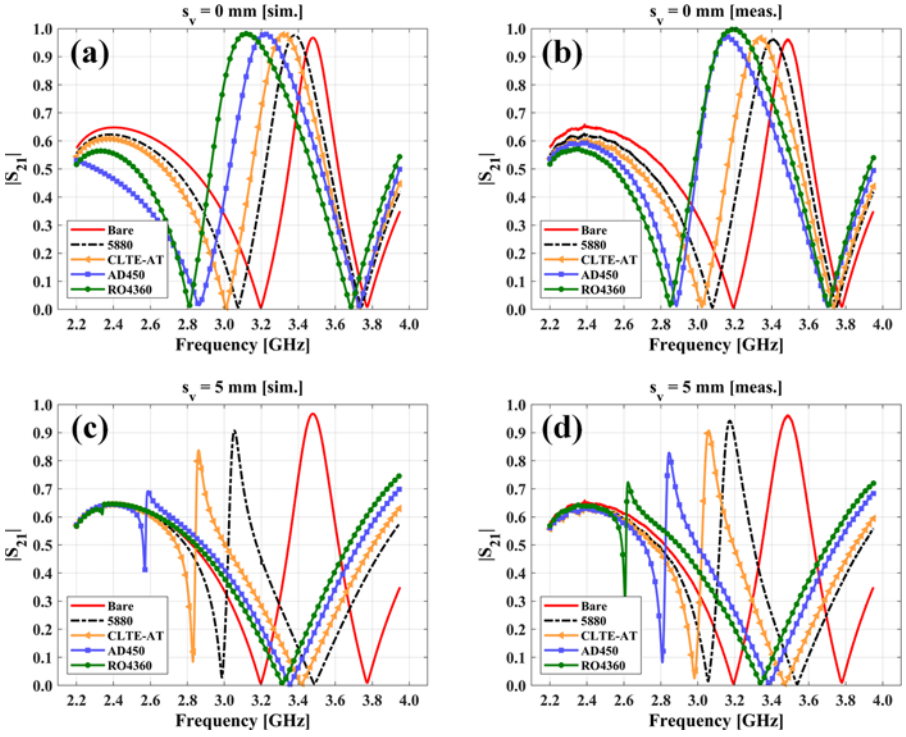

Figure 7. Transmission spectra of the bare and the dielectric-loaded EIT-like metamaterials in vertical sliding application. (a) $s_v = 0$ mm simulations, (b) $s_v = 0$ mm measurements, (c) $s_v = 5$ mm simulations, and (d) $s_v = 5$ mm measurements.

3.195 GHz in measurements, systematically. Alternatively, for VSA at $s_v = 0$ mm, as the real part of relative permittivity of the MUT is changed from bare to RO4360G2™, the frequency of the transmission peak reduces from 3.479 to 3.118 GHz in simulations and from 3.484 to 3.182 GHz in measurements. The behavior of f_0 is very similar for the two applications; however, the transmission bandwidths get effected differently. In more detail, although the transmission bandwidths are nearly the same as the MUT is changed from the bare to RO4360G2™ for HSA at $s_h = 0$ mm, they obviously broaden for VSA at $s_v = 0$ mm. This behavior can be explained by

https://doi.org/10.1017/S175907872300079X Published online by Cambridge University Press

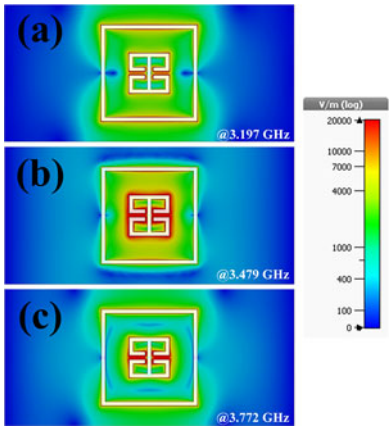

Figure 8. Electric field distribution on the bare EIT-like metamaterial. (a) At 3.197 GHz; the first transmission dip frequency, (b) at 3.479 GHz; the transmission peak frequency, and (c) at 3.772 GHz; the second transmission dip frequency.

the use electric field distributions over the bare EIT-like metamaterial as shown in Fig. 8. First, the electric field distributions at the first null of the EIT-like transmission (i.e., at 3.197 GHz) are especially higher at the top and bottom edges of the CRR and around the gap positions of the ER. Second, the field distributions at the EIT-like transmission peak frequency f_0 (i.e., at 3.479 GHz) are higher mainly on ER but also on the top and bottom edges of the CRR. Moreover, the field distributions are the highest here in strength among the three cases. Lastly, the electric field distributions at the second null of the EIT-like transmission (i.e., at 3.772 GHz) are higher at the gap positions of the ER, on the other hand there are still high electric field distributions around the top and bottom edges of the CRR. However, the field distributions around the top and bottom edges are observed to be significantly reduced as compared with that of the first null. Since in HSA at $s_h = 0$ mm case, the dielectric loadings are along the vertical arms of the CRR (see Fig. 3(a)) and tangent to the gaps of the ER, all the two dips and the transmission peak get effected similarly and simultaneously, and the transmission bandwidth is not affected significantly. However, in VSA at $s_v = 0$ mm case, the dielectric loadings lie in-between the horizontal edges (i.e., top and bottom) of the CRR and the ER. Therefore, the frequencies of the first transmission minimum and the transmission peak slides down more than the second transmission minimum. This application yields a band broadening. As a measure of change in the transmission bandwidth, the quality factor is calculated by Q-factor $= f_0$/FWHM, where FWHM is the full width at half maximum, and it is calculated as the frequency band between the value corresponding to the average of the maximum and minimum values of the transmitted power [62, 63]. Figure 9 shows the calculated Q-factor values by using the simulation and the measurement results for both HSA and VSA at several shift values. Supporting the above observations, for HSA at $s_h = 0$ mm case, Q-factor does not significantly change; however, it gradually decreases for VSA at $s_v = 0$ mm case.

Now, we investigate the behaviors of the EIT-like transmission window in response to the change in real part of relative permittivity of the MUT at the second extremes, i.e., at $s_h = 5$ mm and $s_v = 5$ mm for the HSA and VSA, respectively. For HSA at $s_h = 5$ mm, as the real part of relative permittivity of the MUT is increased from 1 to 6.15 (i.e., from bare to RO4360G2™), f_0 reduces from 3.479 to 2.343 GHz in simulations and reduces from 3.484 to 2.513 GHz in measurements, systematically. Alternatively, for VSA at $s_v = 5$ mm, as the real part of relative permittivity of the MUT is changed from bare to RO4360G2™, the frequency of the transmission peak reduces from 3.479 to 2.393 GHz in simulations and reduces from 3.484 to 2.622 GHz in measurements. Here we have three important observations: First, f_0 of the EIT-like metamaterial becomes more sensitive to the real part of relative permittivity of the dielectric loadings at 5 mm shift cases than that at 0 mm shift cases for both applications. This is not a surprising behavior if we consider Fig. 8 again, since the electric field distribution is highly concentrated on the ER at f_0. At 5 mm shift cases, the dielectric loadings completely cover up the ER, and hence they have greatest effect on the f_0 change, i.e., sensitivity. In literature, the sensitivity (S) is used as a measure which is defined by the ratio difference between the resonance frequencies to the difference between the real part of relative permittivities of the loadings [27, 31–33]. Second, for both HSA and VSA at 5 mm shift cases, as the real part of relative permittivity of the dielectric loadings increases, the overall structure tends to behave like a CRR-only resonator since the resonance frequency of the individual ER reduces much rapidly than that of CRR and the effect of the CRR become more dominant on the transmission characteristics. Ultimately, EIT-like transmission peak almost disappears in the simulations of RO4360G2™-loaded EIT-like metamaterial at $s_v = 5$ mm. There still exists a reduced transmission peak in the related measurement result (see Fig. 7(b)); however, its trend reveals that further increment in the real part of relative permittivity will destroy the EIT-like transmission. Lastly, for 5 mm shift cases, there are obvious changes in the Q-factor observed even by naked eye in Fig. 6(c) and (d) for HSA and in Fig. 7(c) and (d) for VSA. This observation is supported by Fig. 9. In addition to that, Fig. 9 clearly reveals that the Q-factor is dependent on the shift values; however, this dependence is highest in 5 mm shift cases.

The simulation results given in Fig. 10 show that for both HSA and VSA, f_0 chances faster in response to the change in the real part of relative permittivity as the shift amount increases. According to sensitivity, defined above, this means that the sensitivity increases as the shift amount increases and ultimately the sensitivities become maximum for 5 mm shift cases. Moreover, change in f_0 with respect to the real part of relative permittivity change gradually increases with increasing s_h value in HSA. However, it increases significantly in VSA starting with $s_v = 4$ mm. In other words, it can be said that f_0 in HSA is more sensitive than that of VSA to the shift value and the real part of relative permittivity of the dielectric loadings. This observation makes HSA more advantageous in terms of sensitivity and makes it a preferable candidate for a sensing application. On the other hand, Fig. 10 is another indicator showing that the proposed approach is clearly sensitive to the changes in s_h and s_v at fixed relative permittivity values. Although some experimental measurement errors are noticeable, the measurement results in Fig. 10 are consistent with the simulation results.

Table 1 shows the f_0 values obtained by simulations and measurements for $s_h = 5$ mm case of HSA, where f_0 is most dependent on the permittivity of the dielectric loadings ε_r. The data show that the f_0 of HSA for $s_h = 5$ mm is reduced from 3.479 to 2.343 GHz in simulations and it is reduced from 3.484 to 2.513 GHz in measurements as ε_r is increased from 1 to 6.15 which correspond to 1.136 GHz (32.65%) and 0.971 GHz (27.87%) shifts in f_0 in simulations and experiments, respectively.

In this study, we performed analyses in both simulations and experimental measurements. In general, the results show good agreements. However, it is important to discuss here that there are

https://doi.org/10.1017/S175907872300079X Published online by Cambridge University Press

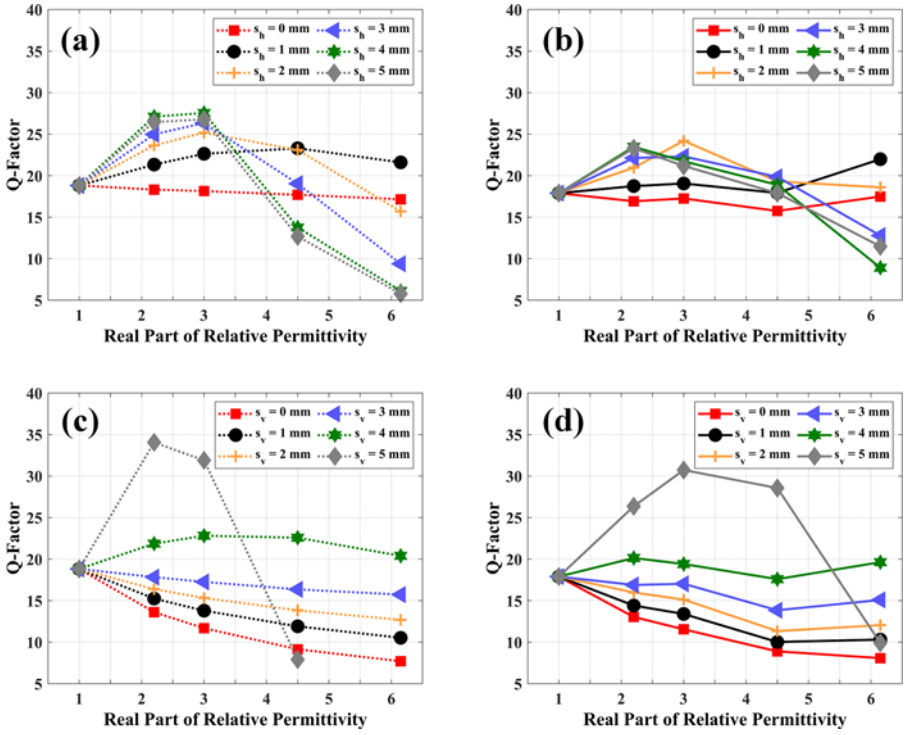

Figure 9. Calculated Q-factors. (a) Horizontal sliding application simulations, (b) horizontal sliding application measurements, (c) vertical sliding application simulations, and (d) vertical sliding application measurements.

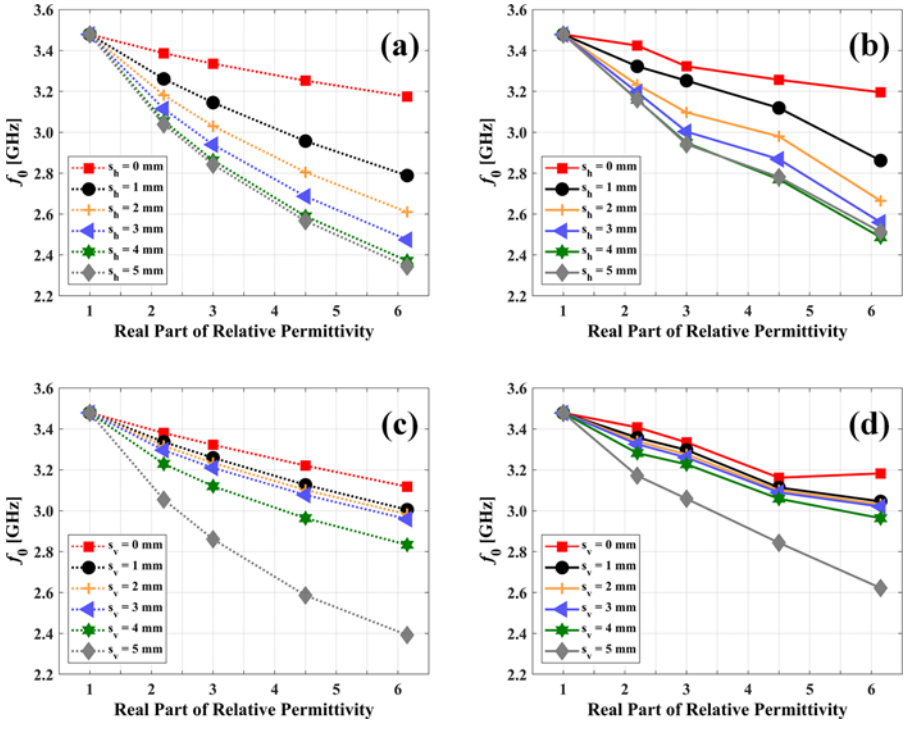

Figure 10. Frequency of transmission peak (i.e., f_0) versus real part of relative permittivity of the dielectric loadings. (a) Horizontal sliding application simulations, (b) horizontal sliding application measurements, (c) vertical sliding application simulations, and (d) vertical sliding application measurements.

some discrepancies in terms of resonance frequencies, transmission amplitudes, or bandwidths. These discrepancies are supposed to be mainly due to the unavoidable additional air gaps between the dielectric loading and the EIT-like metamaterial since the structures do not have ideally flat surfaces. Although using an XPS material in the measurements as a support structure to avoid these additional air gaps is an effective approach depending on our laboratory experiences, it cannot fully provide the ideal simulation setup. Another reason of the discrepancies may be deviations in the dielectric properties of the dielectric loadings with respect to

https://doi.org/10.1017/S175907872300079X Published online by Cambridge University Press

Table 1. Dependence of f_0 on ε_r in the case of $s_h = 5$ mm of horizontal sliding application

Sample	Simulated f_0 (GHz)	Measured f_0 (GHz)	ε_r
Bare	3.479	3.484	1
5880	3.039	3.160	2.2
CLTE-AT™	2.842	2.942	3
AD450	2.566	2.781	4.5
RO4360G2™	2.343	2.513	6.15

the catalog values. We cannot see fabrication errors as a factor here because, there is nearly a perfect agreement between the simulation and experimental results of the bare (unloaded) EIT-like metamaterial.

To complete the study, additional numerical analyses were performed for a fairer comparison with the related literature. This time, the resonator side of the studied EIT-like metamaterial unit cell surface was completely loaded (i.e., covered) with a 10-mm-thick lossless dielectric (i.e., 72.136 mm × 34.036 mm × 10 mm) just on the Rogers RT/duroid® 5880 substrate in the simulation environment. The usage of EIT-like designs for refractive index (n) sensing applications is common [21–26, 53–56]. Therefore, the refractive index of the dielectric is increased from 1 to 1.5, which corresponds to an increase in ε_r from 1 to 2.25, since $n = \sqrt{\varepsilon_r}$ considering $\mu_r = 1$ [23], as the parametric study and transmission spectra are obtained. The simulation results and schematics of the application are shown in Fig. 11. The results reveal that the frequency of transmission peak lowers from 3.479 to 2.841 GHz as the refractive index increases from 1 to 1.5 which corresponds to 0.638 GHz (18.34%) shift in f_0.

To clarify the structural and performance differences of this study as compared to the related EIT-like sensor studies given in the literature, whose mechanism are based on sensing the dielectric constant or refractive index changes of the dielectric loadings (i.e., MUT), Table 2 is presented. The comparison parameters in the table are refractive index n or dielectric constant ε_r range, frequency region, test setup, MUT settling, position adjustability of MUT, and absolute percentage sensitivity (% $|S|$). For Table 2, the % S values are calculated using equation (1) [27].

$$\%S = \frac{\Delta f}{\Delta \varepsilon_r \cdot f_0} \times 100 \quad (1)$$

where $\Delta f = f_2 - f_1$ is the spectral change in the EIT-like peaks in the transmission, $\Delta\varepsilon_r = \varepsilon_{r2} - \varepsilon_{r1}$ is change in the permittivity, and f_0 is EIT-like peak frequency of the bare (i.e., unloaded) case. In the table, given n values are converted to permittivity by using $n = \sqrt{\varepsilon_r}$ considering $\mu_r = 1$ [23]. In the formulation, f_1 corresponds to the resonance frequency where MUT's permittivity is ε_{r1}, and similarly f_2 corresponds to the resonance frequency where MUT's permittivity is ε_{r2}. For the case of $\varepsilon_{r1} = 1$, f_0 will be equal to f_1; however, this is not a requirement as can be seen in reference [25]. If the percentage sensitivity values were given in the articles compared in Table 2, we used it directly, if not, we calculated it by using the data or graphs in the related article. For this reason, there may be small deviations due to reading errors from the graph.

Table 2 reveals that there are three prominent directions of our study. First, the partial coverage of the unit-cell by MUT (i.e., referred to as POR in the table) instead of complete coverage. Second, sensing mechanism based on position adjustability of the MUT, and third, relatively high sensitivity values for the complete coverage scenario (i.e., referred to as COR in the table). The first is believed to be an advantage in sensing applications terms of using small amount of analyte material (i.e., MUT), the second provides an important flexibility for adopting the design in mechanical sensing approaches, and the last is obviously preferred in many sensing applications. For the COR scenario, our EIT-like metamaterial shows 14.67% sensitivity, and it is the second highest percentage sensitivity in the table. For the POR scenario, the sensitivity is reduced in both simulations (6.34%) and experiments (5.41%) as expected with respect to the COR case, since the amount of MUT is reduced. However, these sensitivities are still comparable to references [23, 24, 26] and [27]. In addition to those benefits, we use a rectangular hollow waveguide setup for the characterization of EIT-like sensor performance. The main advantage of the waveguide setup is presenting an array behavior with a single unit cell [61] which again provides an important advantage to reduce the applied total MUT amount.

Conclusion

An EIT-like metamaterial structure operating in the S-band is designed, fabricated, and analyzed numerically and experimentally. Tuning of the EIT-like transmission window is studied by low-volume solid dielectric loadings in two different sliding applications (i.e., HSA and VSA) and for several real part of relative permittivity values of the dielectric loadings from 1 (bare) to 6.15

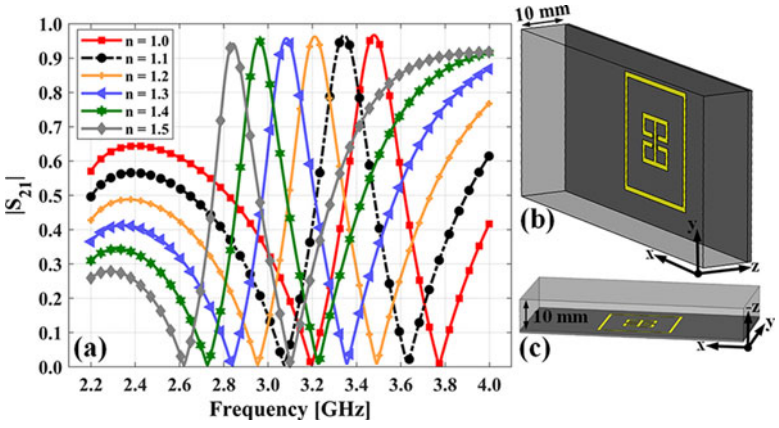

Figure 11. Sensing performance of the 10-mm-thick dielectric-loaded EIT-like metamaterial. (a) Transmission spectra for several refractive indexes. (b) Perspective and (c) side views of 10-mm-thick dielectric-loaded EIT-like metamaterial.

https://doi.org/10.1017/S175907872300079X Published online by Cambridge University Press

Table 2. Comparison of EIT-like sensors in terms of various parameters

Ref.	*n*Range	ε_rRange	Sim./Meas.	Frequency region	Test setup	MUT settling	Position adjustability	Absolute sensitivity |*S*| (%)
[21]	1–1.5	–	Sim.	Microwave	Free space	COR	No	11.06
[22]	1–1.3	–	Sim.	Microwave	Free space	SM	No	16.13
[22]	1–2	–	Sim.	Microwave	Free space	SM	No	10.25
[23]	–	1–3	Sim.	Microwave	Free space	COR	No	7.46
[24]	1–1.3	–	Sim.	Microwave	Free space	SM	No	7.17
[25]	1.332–1.372	–	Meas.	THz	Free space	COR	No	10.64
[26]	1–2.5	–	Sim.	THz	Free space	COR	No	4.1
[27]	–	∼20–80	Meas.	Microwave	MSTL	COR	No	0.05
	–	1–6	Sim.	Microwave	MSTL	COR	No	5
[55]	1–1.4	–	Sim.	THz	Free space	SM	No	9.97
This study	1–1.5	–	Sim.	Microwave	Waveguide	COR	No	14.67
This study	–	1–6.15	Sim.	Microwave	Waveguide	POR	Yes	6.34
This study	–	1–6.15	Meas.	Microwave	Waveguide	POR	Yes	5.41

COR = completely on the resonator, POR = partially on the resonator, SM = surrounding medium, MSTL = microstrip transmission line

(RO4360G2™). In HSA, the dielectric loadings are placed along the vertical edges of the CRR, and in VSA, they are placed along the horizontal edges. The results show that not only the transmission peak frequency f_0 but also the transmission bandwidth (i.e., Q-factor) are sensitive to the real part of relative permittivity and the position of the dielectric loadings for both mechanisms. However, HSA is more sensitive than VSA in terms of both shifting value and the real part of relative permittivity. In HSA for $s_h = 5$ mm case, f_0 is reduced from 3.479 to 2.343 GHz in simulations and it is reduced from 3.484 to 2.513 GHz in measurements as ε_r is increased from 1 to 6.15. These values correspond to 1.136 GHz (32.65%) and 0.971 GHz (27.87%) shifts in f_0 in simulations and experiments, respectively. The results show that HSA is an effective approach to tune the EIT-like transmission window although low-volume dielectric loadings are used. According to the results, 6.34% and 5.41% absolute sensitivities by simulations and measurements, respectively, are the best sensitivity results which are obtained for HSA at 5 mm shift case. In addition, 14.67% sensitivity value is obtained for the complete dielectric loading case in response to the increase in refractive index from 1 to 1.5. The results show that the proposed approach can be easily adapted for position and dielectric constant sensing applications. As the future work, we plan to study on an electrical circuit model for the design to explain the operating principle and the effects of dielectric loadings with another approach.

Acknowledgements. Rogers RT/duroid® 5880, Rogers CLTE-AT™, and Rogers RO4360G2™ material samples were provided courtesy of Rogers Corporation.

Competing interests. None.

References

1. **Harris SE** (1997) Electromagnetically induced transparency. *Physics Today* **50**, 36–42. doi:10.1063/1.881806
2. **Fleischhauer M, Imamoglu A and Marangos JP** (2005) Electromagnetically induced transparency: Optics in coherent media. *Reviews of Modern Physics* **77**, 633–673. doi:10.1103/RevModPhys.77.633
3. **Garrido Alzar CL, Martinez MAG and Nussenzveig P** (2002) Classical analog of electromagnetically induced transparency. *American Journal of Physics* **70**, 37–41. doi:10.1119/1.1412644
4. **Papasimakis N, Fedotov VA, Zheludev NI and Prosvirnin SL** (2008) Metamaterial analog of electromagnetically induced transparency. *Physical Review Letters* **101**, 253903. doi:10.1103/PhysRevLett.101.253903
5. **Hu J, Lang T, Hong Z, Shen C and Shi G** (2018) Comparison of electromagnetically induced transparency performance in metallic and all-dielectric metamaterials. *Journal of Lightwave Technology* **36**, 2083–2093. doi:10.1109/JLT.2018.2804336
6. **Han S, Yang H and Guo L** (2013) Ultra-broadband electromagnetically induced transparency using tunable self-asymmetric planar metamaterials. *Journal of Applied Physics* **114**, 163507. doi:10.1063/1.4826630
7. **Tassin P, Zhang L, Koschny T, Economou EN and Soukoulis CM** (2009) Low-loss metamaterials based on classical electromagnetically induced transparency. *Physical Review Letters* **102**, 053901. doi:10.1103/PhysRevLett.102.053901
8. **Fedotov VA, Rose M, Prosvirnin SL, Papasimakis N and Zheludev NI** (2007) Sharp trapped-mode resonances in planar metamaterials with a broken structural symmetry. *Physical Review Letters* **99**, 147401. doi:10.1103/PhysRevLett.99.147401
9. **Fu Q, Zhang F, Fan Y, Dong J, Cai W, Zhu W, Chen S and Yang R** (2017) Weak coupling between bright and dark resonators with electrical tunability and analysis based on temporal coupled-mode theory. *Applied Physics Letters* **110**, 221905. doi:10.1063/1.4984596
10. **Zhu L, Meng F-Y, Dong L, Wu Q, Che B-J, Gao J, Fu J-H, Zhang K and Yang G-H** (2015) Magnetic metamaterial analog of electromagnetically induced transparency and absorption. *Journal of Applied Physics* **117**, 17D146. doi:10.1063/1.4916189
11. **Zhu L, Meng F-Y, Fu J-H and Wu Q** (2012) An electromagnetically induced transparency metamaterial with polarization insensitivity based on multi-quasi-dark modes. *Journal of Physics D: Applied Physics* **45**, 445105. doi:10.1088/0022-3727/45/44/445105
12. **Yu W, Meng H, Chen Z, Li X, Zhang X, Wang F, Wei Z, Tan C, Huang X and Li S** (2018) The bright–bright and bright–dark mode coupling-based planar metamaterial for plasmonic EIT-like effect. *Optics Communications* **414**, 29–33. doi:10.1016/j.optcom.2017.12.084
13. **Hu S, Liu D and Yang H** (2019) Electromagnetically induced transparency in an integrated metasurface based on bright–dark–bright mode coupling. *Journal of Physics D: Applied Physics* **52**, 175305. doi:10.1088/1361-6463/ab03c3

14. **Hu S, Yang H, Han S, Huang X and Xiao B** (2015) Tailoring dual-band electromagnetically induced transparency in planar metamaterials. *Journal of Applied Physics* **117**, 043107. doi:10.1063/1.4906853
15. **Çetin H and Ekmekçi E** (2020) Electromagnetically induced transparency-like metamaterial design and tuning its transmission window with dielectric cube loadings. In *12th International Conference on Electrical and Electronics Engineering (ELECO) 2020*, Bursa, Turkey, 84–87.
16. **Kang M, Li YN, Chen J, Chen J, Bai Q, Wang HT and Wu PH** (2010) Slow light in a simple metamaterial structure constructed by cut and continuous metal strips. *Applied Physics B* **100**, 699–703. doi:10.1007/s00340-010-4184-6
17. **Lin XQ, Peng J, Chen Z, Yu JW and Yang XF** (2018) A group-delay-based sensor using active EIT-like effect with double sensing applications. *IEEE Sensors Journal* **18**, 9251–9256. doi:10.1109/JSEN.2018.2868873
18. **Nakanishi T, Otani T, Tamayama Y and Kitano M** (2013) Storage of electromagnetic waves in a metamaterial that mimics electromagnetically induced transparency. *Physical Review B* **87**, 161110. doi:10.1103/PhysRevB.87.161110
19. **Bai Y, Chen K, Liu H, Bu T, Cai B, Xu J and Zhu Y** (2015) Optically controllable terahertz modulator based on electromagnetically-induced-transparency-like effect. *Optics Communications* **353**, 83–89. doi:10.1016/j.optcom.2015.05.005
20. **Fan Y, Qiao T, Zhang F, Fu Q, Dong J, Kong B and Li H** (2017) An electromagnetic modulator based on electrically controllable metamaterial analogue to electromagnetically induced transparency. *Scientific Reports* **7**, 40441. doi:10.1038/srep40441
21. **Li R, Kong XK, Liu S-B, Liu Z-M and Li Y-M** (2019) Planar metamaterial analogue of electromagnetically induced transparency for a miniature refractive index sensor. *Physics Letters A* **383**, 125947. doi:10.1016/j.physleta.2019.125947
22. **Tian Y, Hu S, Huang X, Yu Z, Lin H and Yang H** (2017) Low-loss planar metamaterials electromagnetically induced transparency for sensitive refractive index sensing. *Journal of Physics D: Applied Physics* **50**, 405105. doi:10.1088/1361-6463/aa865b
23. **Lin XQ, Chen Z, Yu JW, Liu PQ, Li PF and Chen ZD** (2016) An EIT-based compact microwave sensor with double sensing functions. *IEEE Sensors Journal* **16**, 293–298. doi:10.1109/JSEN.2015.2480800
24. **Shen Z, Wang C and Lu N** (2022) All-dielectric electromagnetically induced transparency-like metasurface with breaking symmetric. *Materials Research Express* **9**, 105801. doi:10.1088/2053-1591/ac9aa4
25. **Liu N, Weiss T, Mesch M, Langguth L, Eigenthaler U, Hirscher M, Sönnichsen C and Giessen H** (2010) Planar metamaterial analogue of electromagnetically induced transparency for plasmonic sensing. *Nano Letters* **10**, 1103–1107. doi:10.1021/nl902621d
26. **Pan W, Yan Y, Ma Y and Shen D** (2019) A terahertz metamaterial based on electromagnetically induced transparency effect and its sensing performance. *Optics Communications* **431**, 115–119. doi:10.1016/j.optcom.2018.09.014
27. **Xu Z, Wang Y and Fang S** (2021) Dielectric characterization of liquid mixtures using EIT-like transmission window. *IEEE Sensors Journal* **21**, 17859–17867. doi:10.1109/JSEN.2021.3085954
28. **Ali L, Wang C, Meng F-Y, Wei Y-C, Tan X, Adhikari KK and Zhao M** (2021) Simultaneous measurement of thickness and permittivity using microwave resonator-based planar sensor. *International Journal of RF and Microwave Computer-Aided Engineering* **31**, e22794. doi:10.1002/mmce.22794
29. **Varshney PK and Akhtar MJ** (2021) Permittivity estimation of dielectric substrate materials via enhanced SIW sensor. *IEEE Sensors Journal* **21**, 12104–12112. doi:10.1109/JSEN.2021.3064923
30. **Gil M, Veléz P, Aznar-Ballesta F, Muñoz-Enano J and Martín F** (2020) Differential sensor based on electroinductive wave transmission lines for dielectric constant measurements and defect detection. *IEEE Transactions on Antennas and Propagation* **68**, 1876–1886. doi:10.1109/TAP.2019.2938609
31. **Liu Q, Deng H, Meng P and Sun H** (2021) High sensitivity sensor loaded with octagonal spiral resonators for retrieval of solid material permittivity. *IEEE Sensors Journal* **21**, 20010–20017. doi:10.1109/JSEN.2021.3099298
32. **Ebrahimi A, Scott J and Ghorbani K** (2018) Differential sensors using microstrip lines loaded with two split-ring resonators. *IEEE Sensors Journal* **18**, 5786–5793. doi:10.1109/JSEN.2018.2840691
33. **Ebrahimi A, Scott J and Ghorbani K** (2018) Transmission lines terminated with LC resonators for differential permittivity sensing. *IEEE Microwave and Wireless Components Letters* **28**, 1149–1151. doi:10.1109/LMWC.2018.2875996
34. **Wang C, Ali L, Meng F-Y, Adhikari KK, Zhou ZL, Wei YC, Zou DQ and Yu H** (2021) High-accuracy complex permittivity characterization of solid materials using parallel interdigital capacitor-based planar microwave sensor. *IEEE Sensors Journal* **21**, 6083–6093. doi:10.1109/JSEN.2020.3041014
35. **Raveendran A and Raman S** (2021) Low cost multifunctional planar RF sensors for dielectric characterization and quality monitoring. *IEEE Sensors Journal* **21**, 24056–24065. doi:10.1109/JSEN.2021.3114257
36. **Varshney PK, Kapoor A and Akhtar MJ** (2021) Highly sensitive ELC resonator based differential sensor. *IEEE Transactions on Instrumentation and Measurement* **70**, 8004710. doi:10.1109/TIM.2021.3113135
37. **Kiani S, Rezaei P, Navaei M and Abrishamian MS** (2018) Microwave sensor for detection of solid material permittivity in single/multilayer samples with high quality factor. *IEEE Sensors Journal* **18**, 9971–9977. doi:10.1109/JSEN.2018.2873544
38. **Ebrahimi A, Beziuk G, Scott J and Ghorbani K** (2020) Microwave differential frequency splitting sensor using magnetic-LC resonators. *Sensors* **20**, 1066. doi:10.3390/s20041066
39. **Ali L, Wang C, Meng F-Y, Adhikari KK, Wei Y-C, Li J-H, Song Z-W and Zhao M** (2021) Design and optimization of interdigitated microwave sensor for multidimensional sensitive characterization of solid materials. *IEEE Sensors Journal* **21**, 22814–22822. doi:10.1109/JSEN.2021.3105410
40. **Chiam S-Y, Singh R, Rockstuhl C, Lederer F, Zhang W and Bettiol AA** (2009) Analogue of electromagnetically induced transparency in a terahertz metamaterial. *Physical Review B* **80**, 153103. doi:10.1103/PhysRevB.80.153103
41. **Lin XQ, Yu JW, Jiang Y, Jin JY and Fan Y** (2012) Electromagnetically induced transparencies in a closed waveguide with high efficiency and wide frequency band. *Applied Physics Letters* **101**, 093502. doi:10.1063/1.4748121
42. **Padilla WJ, Aronsson MT, Highstrete C, Lee M, Taylor AJ and Averitt RD** (2007) Electrically resonant terahertz metamaterials: Theoretical and experimental investigations. *Physical Review B* **75**, 041102. doi:10.1103/PhysRevB.75.041102
43. **Powell DA, Shadrivov IV and Kivshar YS** (2009) Nonlinear electric metamaterials. *Applied Physics Letters* **95**, 084102. doi:10.1063/1.3212726
44. **Arritt B, Adomanis B, Khraishi T and Smith D** (2010) Parametric analysis of the strain-dependent behavior of a metamaterial electric resonator. *Applied Physics Letters* **97**, 191907. doi:10.1063/1.3507892
45. **Liu R, Degiron A, Mock JJ and Smith DR** (2007) Negative index material composed of electric and magnetic resonators. *Applied Physics Letters* **90**, 263504. doi:10.1063/1.2752120
46. **Landy NI, Sajuyigbe S, Mock JJ, Smith DR and Padilla WJ** (2008) Perfect metamaterial absorber. *Physical Review Letters* **100**, 207402. doi:10.1103/PhysRevLett.100.207402
47. **Tao H, Landy NI, Bingham CM, Zhang X, Averitt RD and Padilla WJ** (2008) A metamaterial absorber for the terahertz regime: Design, fabrication and characterization. *Optics Express* **16**, 7181–7188. doi:10.1364/OE.16.007181
48. **Ozden K, Yucedag OM and Kocer H** (2016) Metamaterial based broadband RF absorber at X-band. *AEU - International Journal of Electronics and Communications* **70**, 1062–1070. doi:10.1016/j.aeue.2016.05.002
49. **Albishi AM and Ramahi OM** (2018) Highly sensitive microwaves sensors for fluid concentration measurements. *IEEE Microwave and Wireless Components Letters* **28**, 287–289. doi:10.1109/LMWC.2018.2805866
50. **Chin JY, Lu M and Cui TJ** (2008) Metamaterial polarizers by electric-field-coupled resonators. *Applied Physics Letters* **93**, 251903. doi:10.1063/1.3054161
51. **Bala BD, Rahim MKA and Murad NA** (2014) Small electrical metamaterial antenna based on coupled electric field resonator with enhanced bandwidth. *Electronics Letters* **50**, 138–139. doi:10.1049/el.2013.3884

https://doi.org/10.1017/S175907872300079X Published online by Cambridge University Press

52. **Chen X, Cheng S, Liang Y, Zhan S, Nie G, Cao S, Ding S and Gao Y** (2019) Observation of EIT-like effect in plasmonic metasurface based on the modulation of bright–bright mode coupling. *Optics Communications* **453**, 124313. doi:10.1016/j.optcom.2019.07.075
53. **Gao F, Yuan P, Gao S, Deng J, Sun Z, Jin G, Zeng G and Yan B** (2021) Active electromagnetically induced transparency effect in graphene-dielectric hybrid metamaterial and its high-performance sensor application. *Nanomaterials* **11**, 2032. doi:10.3390/nano11082032
54. **Yang M, Liang L, Zhang Z, Xin Y, Wei D, Song X, Zhang H, Lu Y, Wang M, Zhang M, Wang T and Yao J** (2019) Electromagnetically induced transparency-like metamaterials for detection of lung cancer cells. *Optics Express* **27**, 19520–19529. doi:10.1364/OE.27.019520
55. **Ma T, Huang Q, He H, Zhao Y, Lin X and Lu Y** (2019) All-dielectric metamaterial analogue of electromagnetically induced transparency and its sensing application in terahertz range. *Optics Express* **27**, 16624–16634. doi:10.1364/OE.27.016624
56. **Meng F-Y, Wu Q, Erni D, Wu K and Lee J** (2012) Polarization-independent metamaterial analog of electromagnetically induced transparency for a refractive-index-based sensor. *IEEE Transactions on Microwave Theory and Techniques* **60**, 3013–3022. doi:10.1109/TMTT.2012.2209455
57. **Qin M, Pan C, Chen Y, Ma Q, Liu S, Wu E and Wu B** (2018) Electromagnetically induced transparency in all-dielectric U-shaped silicon metamaterials. *Applied Sciences* **8**, 1799. doi:10.3390/app8101799
58. (2023) CST STUDIO SUITE®, Dassault Systèmes, the 3DEXPERIENCE® Company. www.3ds.com/products-services/simulia/products/cst-studio-suite/.
59. **Ekmekci E, Kose U, Cinar A, Ertan O and Ekmekci Z** (2019) The use of metamaterial type double-sided resonator structures in humidity and concentration sensing applications. *Sensors and Actuators A: Physical* **297**, 111559. doi:10.1016/j.sna.2019.111559
60. **Pozar DM** (2011) *Microwave Engineering*, 4th. Hoboken, NJ: John Wiley & Sons, Inc.
61. **Karacan N, Ekmekci E and Turhan-Sayan G** (2020) Response to "Comment on 'Sliding planar conjoined cut-wire-pairs: A novel approach for splitting and controlling the absorption spectra'" [J. Appl. Phys. 128, 126101 (2020)]. *Journal of Applied Physics* **128**, 126102. doi:10.1063/5.0018386
62. **Christopoulos T, Tsilipakos O, Sinatkas G and Kriezis EE** (2019) On the calculation of the quality factor in contemporary photonic resonant structures. *Optics Express* **27**, 14505–14522. doi:10.1364/OE.27.014505
63. **Tang Y, Zhang Z, Wang R, Hai Z, Xue C, Zhang W and Yan S** (2017) Refractive index sensor based on fano resonances in metal-insulator-metal waveguides coupled with resonators. *Sensors* **17**, 784. doi:10.3390/s17040784

Hasan Cetin received his B.Sc. and M.Sc. degrees in electronics and communication engineering from Suleyman Demirel University, Isparta, Turkey, in 2017 and 2021, respectively. He is currently a Ph.D. candidate and working as a research assistant in the Department of Electrical and Electronics Engineering at Suleyman Demirel University, Isparta, Turkey. His research areas include metamaterials and microwave sensors.

Evren Ekmekci received his B.Sc. degree in electronics and communication engineering from Suleyman Demirel University, Isparta, Turkey, in 2002 and his Ph.D. degree in electrical and electronics engineering from Middle East Technical University, Ankara, Turkey, in 2010. He is currently working as a professor in the Department of Electrical and Electronics Engineering, Suleyman Demirel University, Isparta, Turkey. His current research interests include dielectric resonators, metamaterials, and antennas.

https://doi.org/10.1017/S175907872300079X Published online by Cambridge University Press